


Structural properties of ${}^4\text{He}_N$ ($N = 2\text{--}10$) clusters for different potential models at the physical point and at unitarity

A. J. Yates and D. Blume 

Homer L. Dodge Department of Physics and Astronomy, The University of Oklahoma, 440 W. Brooks Street, Norman, Oklahoma 73019, USA
and Center for Quantum Research and Technology, The University of Oklahoma, 440 W. Brooks Street, Norman, Oklahoma 73019, USA



(Received 11 November 2021; accepted 3 February 2022; published 25 February 2022)

Since the ${}^4\text{He}$ dimer supports only one weakly bound state with an average interatomic distance much larger than the van der Waals length and no deeply bound states, ${}^4\text{He}_N$ clusters with $N > 2$ are a paradigmatic model system with which to explore foundational concepts such as large s -wave scattering length universality, van der Waals universality, Efimov physics, and effective field theories. This work presents structural properties such as the pair and triple distribution functions, the hyper-radial density, the probability to find the N th particle at a given distance from the center of mass of the other $N - 1$ atoms, and selected contacts. The kinetic energy release, which can be measured via Coulomb explosion in dedicated size-selected molecular beam experiments—at least for small N —is also presented. The structural properties are determined for three different realistic ${}^4\text{He}$ - ${}^4\text{He}$ interaction potentials and contrasted with those for an effective low-energy potential model from the literature that reproduces the energies of ${}^4\text{He}_N$ clusters in the ground state for $N = 2$ to $N = \infty$ at the $\gtrsim 95\%$ level with just four input parameters. The study is extended to unitarity (infinite s -wave scattering length) by artificially weakening the interaction potentials. In addition to contributing to the characterization of small bosonic helium quantum droplets, our study provides insights into the effective low-energy theory's predictability of various structural properties.

DOI: [10.1103/PhysRevA.105.022824](https://doi.org/10.1103/PhysRevA.105.022824)

I. INTRODUCTION

Bosonic helium droplets, i.e., clusters consisting of a finite number of ${}^4\text{He}$ (helium-4) atoms, have captivated physicists' interest over many decades [1–34]. They provide a bridge between the microscopic and macroscopic worlds, with the helium dimer being bound by just 1.6 mK [35,36] and the binding energy per particle reaching about 7 K in bulk liquid helium-4 [37]. Mesoscopic helium-4 droplets are essentially incompressible and a subset of their properties is captured accurately by a “bare bone” liquid drop model, which contains a volume term, a surface term, and two additional terms that are treated as fitting parameters [12]. We note that liquid drop models that contain volume, surface, Coulomb, pairing, and asymmetry terms provide a starting point for understanding key properties of nuclei, including the stability of highly deformed nuclei and nuclear fission [38]. The roton minimum, the smoking gun of superfluid bulk helium-4 [39,40], has been found theoretically to first emerge for $N \approx 60$ atoms [41], motivating the term microscopic superfluidity. Experimentally, the prediction was verified by embedding a small helium-4 cluster of varying size into a much larger helium-3 droplet [42]. Large helium-4 droplets with more than about $N = 1000$ atoms, in turn, have been employed as microlaboratories with which to capture, cool, and equilibrate impurities of varying size, from single atoms to proteins [43–49].

This paper provides a detailed analysis of various observables of small pristine ${}^4\text{He}_N$ clusters, $N = 2\text{--}10$, that interact either through a sum of realistic two-body potentials [50–52]

or an effective low-energy model potential that includes two- and three-body terms [33]. Emphasis is placed on structural properties, including the long-distance tail and the short-distance correlations (on the scale of the van der Waals length r_{vdW}) of the pair, Jacobi, and hyper-radial distribution functions. The long-distance tails are expected to be governed by the effective low-energy model, i.e., the large-distance fall-off should be fully governed by the binding energy, which was matched for $N = 2\text{--}4$ when constructing the effective low-energy model and reproduces the exact binding energies at the $\gtrsim 95\%$ level for $N > 4$ [33].

The short-distance correlations are expected to be governed by the two-body wave function for an attractive van der Waals potential, i.e., a potential with $-C_6/r^6$ tail [53,54]. For helium clusters that have been “artificially” scaled to the unitary point, this has previously been confirmed through dedicated calculations [53,54]. For the physical point, this is demonstrated in this work. The collapse of the pair, triple, and higher-order distribution functions for interatomic distances around $r \approx r_{\text{vdW}}$ was noted in the literature, motivating the adaption of the n -body Tan contact ($n = 2, 3, \dots$) [55–60] to quantum clusters that exhibit weak universality (two-body potentials with van der Waals tail and strongly repulsive hard-wall-like short-distance repulsion) [34]. This work compares the two-body contact with results from the literature and additionally introduces a $(2 + 1)$ contact. We note that short-distance correlations, or generalizations of the Tan contact from zero- to finite-range interactions, are also being actively investigated in nuclei [61–65].

Since the effective low-energy potential model does not “know” about r_{vdW} , the short-distance or high-energy correlations are not captured by that model despite the fact that the short-distance physics is universal, i.e., governed by the s -wave scattering length a_s and the van der Waals length r_{vdW} . Thus, the development of a low-energy van der Waals theory is highly desirable. While this is beyond the scope of the present paper, we note that first steps in this direction were recently taken [66]. Our aim in the present work is to provide a careful analysis of the different “universality regimes,” providing a comprehensive study of the structural properties of pristine helium-4 clusters at the physical point and at unitarity.

Many naturally occurring systems are characterized by competing length or energy scales. The helium-helium interaction is unique in that its naturally occurring s -wave scattering length a_s is more than an order of magnitude larger than its effective range. Even though a_s is large, it is not infinitely large. The regime where a_s goes to infinity and the effective range goes to zero has been studied quite extensively, not only in the context of bosons but also in the context of fermions. Correspondingly, a comparison of the behaviors of small helium clusters at the physical point and those of helium clusters at unitarity provides insights into developing universal van der Waals theories. The lessons learned have importance beyond atomic droplets—some findings carry over to the nuclear chart, with the weakly bound triton, alpha-particle, and halo-nuclei playing loose analogs of weakly bound atomic clusters.

The remainder of this paper is organized as follows. Section II introduces the system Hamiltonian, describes the numerical techniques employed to solve the time-independent Schrödinger equation for clusters consisting of up to $N = 10$ atoms, and defines several structural observables of interest. Section III presents and interprets our results. Connections with the literature are established throughout. Finally, Sec. IV summarizes and offers an outlook.

II. THEORETICAL BACKGROUND

A. Hamiltonian

Each ${}^4\text{He}$ atom is treated as a point particle with position vector \vec{r}_j ($j = 1, \dots, N$) and mass m [67]. The nonrelativistic N -atom Hamiltonian \hat{H} reads

$$\hat{H} = \sum_{j=1}^N \frac{-\hbar^2}{2m} \nabla_{\vec{r}_j}^2 + V_{\text{int}}(r_{1,2}, \dots, r_{N-1,N}). \quad (1)$$

The interaction potential V_{int} depends on the interatomic distances $r_{j,k}$, where $r_{j,k}$ is equal to $|\vec{r}_j - \vec{r}_k|$. We consider two different classes of interaction potentials V_{int} , referred to as model I and model II. For model I, V_{int} consists of a sum over two-body Born-Oppenheimer potentials $V_{\text{BO}}(r_{j,k})$, which have a repulsive core at small interatomic distances due to the electron repulsion and Pauli exclusion principle and an attractive van der Waals tail with leading-order term $-C_6/(r_{j,k})^6$,

$$V_{\text{int}}(r_{1,2}, \dots, r_{N-1,N}) = \sum_{j=1}^{N-1} \sum_{k>j}^N V_{\text{BO}}(r_{j,k}). \quad (2)$$

Calculations for model I are performed for three variants; specifically, we consider the Born-Oppenheimer potentials by Aziz *et al.* [50] (HFD-HE2 potential, model IA), Cencek *et al.* [51] (CPKMJS potential, model IB), and Tang *et al.* [52] (TTY potential, model IC).

For model II, V_{int} is taken to be the effective low-energy potential developed by Kievsky *et al.* [31,33],

$$V_{\text{int}}(r_{1,2}, \dots, r_{N-1,N}) = \sum_{j=1}^{N-1} \sum_{k>j}^N V_{2,G}(r_{j,k}) + \sum_{j=1}^{N-2} \sum_{k>j}^{N-1} \sum_{l>k}^N V_{3,G}(R_{j,k,l}), \quad (3)$$

where $V_{2,G}(r_{j,k})$ and $V_{3,G}(R_{j,k,l})$ denote two- and three-body Gaussian potentials,

$$V_{2,G}(r_{j,k}) = w_0 \exp[-(r_{j,k}/r_0)^2] \quad (4)$$

and

$$V_{3,G}(R_{j,k,l}) = W_0 \exp[-(R_{j,k,l}/R_0)^2], \quad (5)$$

with

$$R_{j,k,l}^2 = \frac{1}{9}(r_{j,k}^2 + r_{j,l}^2 + r_{k,l}^2). \quad (6)$$

Reference [33] adjusted the parameters w_0 , r_0 , W_0 , and R_0 such that the low-energy Hamiltonian reproduces the “exact” two-body s -wave scattering length and the $N = 2, 3$, and 4 ground-state energies of the realistic HFD-HE2 Born-Oppenheimer potential (model IA) [68]. While the two-body potential $V_{2,G}$ is attractive for all distances $r_{j,k}$ (i.e., w_0 is negative), the three-body potential is purely repulsive for all hyper-radii $R_{j,k,l}$ (i.e., W_0 is positive). The effective three-body repulsion “counteracts” the strong short-distance attraction of $V_{2,G}$. For $W_0 = 0$, the Gaussian interaction model yields a ground-state energy that scales as N^2 [30,69]. The finite repulsive three-body term changes the scaling for N up to about 10 to approximately N [31,33,69,70], in agreement with what is being observed for the realistic interaction potentials (model IA, model IB, and model IC).

The ${}^4\text{He}$ - ${}^4\text{He}$ potential is characterized by a large s -wave scattering, i.e., a scattering length that is about 35 to 45 times larger than the van der Waals length r_{vdW} , $r_{\text{vdW}} \approx 5 a_0$ (the exact ratio depends on the interaction potential); see, e.g., Refs. [18,71]. We employ the definition $r_{\text{vdW}} = (mC_6/\hbar^2)^{1/4}/2$. The scale separation is a key requirement for the emergence of Efimov physics in the three-body sector [72–74]. Indeed, the first-excited state of the ${}^4\text{He}$ trimer, which has been probed experimentally [26], has been identified as an essentially pure Efimov state, i.e., a state that can be described with high accuracy by just two input parameters (the s -wave scattering length and a three-body parameter) [4,5,8,23,25,27,29,72]. In contrast, finite-range effects enter into the description of the ${}^4\text{He}$ trimer ground state [25,26,75]. Despite this, the low-energy model (model II) reproduces the ground-state energies of ${}^4\text{He}_N$ clusters with $N = 2$ to $N = \infty$ remarkably well (i.e., at the $\gtrsim 95\%$ level) [33].

To investigate the regime where the two-body s -wave scattering length a_s diverges, we follow the literature and scale V_{int} by λ ($\lambda < 1$); we do this for model IA and model IB, choosing

TABLE I. Ground-state energies, in atomic units (columns 2–5), and selected energy ratios, in percent (columns 6 and 7), at the physical point for various interaction models. The two-body s -wave scattering lengths are $a_s = 234.84, 170.86, 188.20,$ and $235.24 a_0$ for model IA, model IB, model IC, and model II, respectively. ^(a) The $N = 2$ energies are calculated using a grid-based approach. The extrapolated zero imaginary time-step DMC growth energies are $-2.638(10) \times 10^{-9}, -5.11(3) \times 10^{-9}, -4.166(10) \times 10^{-9},$ and $-2.632(6) \times 10^{-9}$ a.u. for model IA, model IB, model IC, and model II, respectively. The comparatively large errors for the $N = 2$ DMC energies are due to the large fluctuations associated with extremely weakly bound systems. ^(b) For $N = 3$, extrapolated zero imaginary time-step DMC growth energies are reported. ^(c) For $N = 4$ –10, finite imaginary time-step DMC growth energies are reported; the errors only account for the statistical uncertainty and not for the extrapolation error (the extrapolation to the zero imaginary time step is estimated to lead to a correction that is smaller than 0.5%). ^(d) The HFD-HE2 energies differ slightly from those reported in Ref. [33] due to the difference in m [67]. When we use the same mass as Ref. [33], our energies agree within errors with those of Ref. [33].

N	$E_{\text{HFD-HE2}}^{(d)}$ (Model IA)	E_{CPKMJS} (Model IB)	E_{TTY} (Model IC)	E_{GAUSS} (Model II)	$E_{\text{CPKMJS}}/E_{\text{HFD-HE2}}$ (in percent)	$E_{\text{GAUSS}}/E_{\text{HFD-HE2}}$ (in percent)
2 ^(a)	-2.645×10^{-9}	-5.147×10^{-9}	-4.183×10^{-9}	-2.6357×10^{-9}	195	100
3 ^(b)	$-3.713(3) \times 10^{-7}$	$-4.174(5) \times 10^{-7}$	$-4.006(3) \times 10^{-7}$	$-3.715(1) \times 10^{-7}$	112	100
4 ^(c)	$-1.688(1) \times 10^{-6}$	$-1.815(1) \times 10^{-6}$	$-1.768(1) \times 10^{-6}$	$-1.6984(1) \times 10^{-6}$	108	101
5 ^(c)	$-3.966(1) \times 10^{-6}$	$-4.201(1) \times 10^{-6}$	$-4.112(1) \times 10^{-6}$	$-3.9622(3) \times 10^{-6}$	106	100
6 ^(c)	$-7.102(2) \times 10^{-6}$	$-7.467(2) \times 10^{-6}$	$-7.325(1) \times 10^{-6}$	$-7.0166(4) \times 10^{-6}$	105	99
7 ^(c)	$-1.0986(5) \times 10^{-5}$	$-1.150(1) \times 10^{-5}$	$-1.130(1) \times 10^{-5}$	$-1.0737(1) \times 10^{-5}$	106	98
8 ^(c)	$-1.5531(6) \times 10^{-5}$	$-1.621(1) \times 10^{-5}$	$-1.594(1) \times 10^{-5}$	$-1.5030(1) \times 10^{-5}$	104	97
9 ^(c)	$-2.066(1) \times 10^{-5}$	$-2.152(1) \times 10^{-5}$	$-2.1176(8) \times 10^{-5}$	$-1.9830(2) \times 10^{-5}$	104	96
10 ^(c)	$-2.631(1) \times 10^{-5}$	$-2.736(1) \times 10^{-5}$	$-2.694(1) \times 10^{-5}$	$-2.5083(2) \times 10^{-5}$	104	95

λ such that the s -wave scattering length of V_{BO} is infinitely large. For model IA, we use $\lambda = 0.9792445$ [33]; because our mass is slightly different than that used in Ref. [33], the resulting scattering length is large but not infinitely large ($1/a_s \approx 10^{-5} a_0^{-1}$). For model IB, we use $\lambda = 0.9713665$ [25], resulting in $1/a_s \approx 10^{-7} a_0^{-1}$. We note that the scaling changes the van der Waals length and effective range of V_{BO} only slightly [76]. For model II, we again use the parameters from Kievsky *et al.* [33]; while r_0 and R_0 remain the same as at the physical point, $|w_0|$ and W_0 are, respectively, slightly smaller and slightly larger at unitarity than at the physical point. As stated, the scaling factors λ and the parameters of the effective low-energy model are taken from the literature. Since the m values employed in the literature differ, the resulting scattering lengths are very large but not infinitely large; we emphasize that this does not impact the conclusions of the paper.

B. Monte Carlo techniques

Our $N \geq 3$ results are obtained by the diffusion Monte Carlo (DMC) method [77–79], which yields the ground-state energies and structural properties of the ground state. The DMC method with importance sampling utilizes a guiding or trial wave function ψ_T that is optimized using the variational Monte Carlo (VMC) technique [80]. The nodeless guiding or trial wave function ψ_T , which depends on a set of non-linear variational parameters \vec{p} , is optimized by minimizing the energy expectation value, which is evaluated stochastically using Metropolis sampling [81]. If the walker number is sufficiently large and the imaginary time step τ sufficiently small, the DMC energies are, within statistical uncertainties, exact. We use between 2000 and 5000 walkers for all N considered. The energy is calculated using the growth estimator and the mixed estimator, yielding the growth energy E_g and the

mixed energy E_m , respectively. For the calculations reported in Tables I and II, the two estimators yield consistent energies, i.e., the distribution of the energies and errors are consistent with the fact that the errors indicate a 68% confidence interval. For $N = 2$, a statistically significant time-step dependence is observed (see Fig. S1 in the Supplemental Material [82] for details); the caption of Table I reports the extrapolated zero imaginary time-step energies E_g . The time-step dependence for $N = 3$ is smaller than for $N = 2$, but still, at least for models IA–IC, statistically significant (see Fig. S2 of the Supplemental Material [82]). Correspondingly, Tables I and II report extrapolated zero imaginary time-step growth energies E_g . For $N > 3$, the time-step dependence is estimated to be smaller than 0.5% and Tables I and II report growth energies that are obtained for a fixed imaginary time-step (τ between 200 and 400 a.u., where a.u. stands for atomic units).

To obtain essentially unbiased structural properties, we use the “forward walking (tagging) scheme” introduced in Refs. [83,84]. We find that the structural properties calculated in this manner agree, except for regimes where the sampling probability is extremely low, with those obtained by subtracting the VMC estimate $\langle \hat{A} \rangle_{\text{VMC}}$ from twice the mixed DMC estimate $\langle \hat{A} \rangle_{\text{DMC}}$ [83]; here, $\langle \hat{A} \rangle_{\text{VMC}}$ and $\langle \hat{A} \rangle_{\text{DMC}}$ denote expectation values of the operator \hat{A} that are calculated with respect to $|\psi_T|^2$ and $\psi_T \Psi_0$, respectively, where Ψ_0 denotes the exact real ground-state wave function.

The trial wave function ψ_T is taken to be of the Bijl-Jastrow form for all four models [7,21,80],

$$\psi_T(r_{1,2}, \dots, r_{N-1,N}) = \prod_{j=1}^{N-1} \prod_{k>j}^N \exp[f(r_{j,k})]. \quad (7)$$

For model I, the two-body correlation function $f(r_{j,k})$ contains five variational parameters ($p_\alpha, p_\beta, p_\gamma, p_0,$ and p_1) that

TABLE II. Ground-state energies, in atomic units (columns 2–4), and selected energy ratios, in percent (columns 5 and 6), at unitarity for various interaction models. The superscripts (b)–(d) have the same meaning as in Table I.

N	$E_{\text{HFD-HE2}}^{(d)}$ (Model IA)	E_{CPKMIS} (Model IB)	E_{GAUSS} (Model II)	$E_{\text{CPKMIS}}/E_{\text{HFD-HE2}}$ (in percent)	$E_{\text{GAUSS}}/E_{\text{HFD-HE2}}$ (in percent)
3 ^(b)	$-2.656(6) \times 10^{-7}$	$-2.65(1) \times 10^{-7}$	$-2.665(1) \times 10^{-7}$	100	100
4 ^(c)	$-1.391(1) \times 10^{-6}$	$-1.395(5) \times 10^{-6}$	$-1.4028(1) \times 10^{-6}$	100	101
5 ^(c)	$-3.411(3) \times 10^{-6}$	$-3.418(4) \times 10^{-6}$	$-3.4130(2) \times 10^{-6}$	100	100
6 ^(c)	$-6.235(6) \times 10^{-6}$	$-6.241(4) \times 10^{-6}$	$-6.1642(4) \times 10^{-6}$	100	99
7 ^(c)	$-9.764(9) \times 10^{-6}$	$-9.773(4) \times 10^{-6}$	$-9.5379(6) \times 10^{-6}$	100	98
8 ^(c)	$-1.391(1) \times 10^{-5}$	$-1.392(8) \times 10^{-5}$	$-1.3446(1) \times 10^{-5}$	100	97
9 ^(c)	$-1.861(1) \times 10^{-5}$	$-1.863(10) \times 10^{-5}$	$-1.7824(1) \times 10^{-5}$	100	96
10 ^(c)	$-2.379(2) \times 10^{-5}$	$-2.382(12) \times 10^{-5}$	$-2.2626(2) \times 10^{-5}$	100	95

are optimized for each N ,

$$f_{\text{I}}(r) = -p_{\alpha}r^{-\alpha} - p_{\beta}r^{-\beta} - p_{\gamma}r^{-\gamma} - p_0 \ln(r) - p_1 r. \quad (8)$$

Two combinations for α , β , and γ are considered. The first combination ($\alpha = 5$, $\beta = 4$, and $\gamma = 2$) is similar to what has been used frequently in the literature [7,21,80], namely, the same α and γ , but $\beta = 0$. The second combination ($\alpha = 4.6$, $\beta = 1.2$, and $\gamma = 0$) was found to result in comparable or lower variational energies with one less variational parameter.

Table S1 in the Supplemental Material [82] reports the variational parameters for model IB, using $\alpha = 4.6$, $\beta = 1.2$, and $\gamma = 0$ for all N . The VMC energy E_{VMC} for $N \geq 4$ reaches between 91% and 96% of the DMC energy at the physical point and between 91% and 97% of the DMC energy at unitarity.

The pair correlation function for the effective low-energy model (model II) is known to differ from that for the van der Waals potentials. Correspondingly, the functional form of the correlation function needs to be adjusted to capture the short-distance characteristics of the two-body Gaussian potential. For model II, the two-body correlation function $f(r_{j,k})$ takes the form

$$f_{\text{II}}(r) = \begin{cases} -\sum_{k=3}^8 p_k r^{k-7} - p_9 \ln(r) & \text{for } r > r_m \\ -p_2 r^2 & \text{for } r < r_m. \end{cases} \quad (9)$$

The parameters p_3 and p_7 are chosen such that $f_{\text{II}}(r)$ and its first derivative with respect to r are continuous at $r = r_m$; the matching distance r_m and the parameters p_2 , p_4 , p_5 , p_6 , p_8 , and p_9 are optimized for each N by minimizing the energy (see Table S2 in the Supplemental Material [82]). The VMC energy E_{VMC} for $N \geq 4$ reaches between 97% and 98% of the DMC energy at both the physical point and at unitarity.

For both the realistic van der Waals and low-energy models, we checked carefully that the structural properties are independent of the trial wave function. Specifically, we compared results for fully optimized and not fully optimized parameters and we compared structural properties obtained by the VMC method, the mixed estimator, and a forward walking scheme (see next section).

C. Structural observables

This section defines several structural observables that are analyzed in Sec. III as a function of N for different V_{int} . As mentioned above, our DMC implementation determines the

structural properties using a forward walking scheme that ensures that the excited-state contributions contained in the mixed density $\psi_T \Psi_0$ decay prior to measuring the observable during the DMC run.

The pair distribution function $P_N^{(2)}(r)$ of the N -body cluster, which has units of $(\text{length})^{-3}$ and is normalized according to

$$\int_0^{\infty} P_N^{(2)}(r) r^2 dr = 1, \quad (10)$$

is obtained by calculating the expectation value of the operator $\hat{P}_N^{(2)}(r)$,

$$\hat{P}_N^{(2)}(r) = \frac{2}{N(N-1)} \sum_{j=1}^{N-1} \sum_{k>j}^N \frac{\delta(r_{j,k} - r)}{r^2}. \quad (11)$$

The short-distance behavior of $P_N^{(2)}(r)$ enters into the definition of the r -independent scalar two-body contact $C_N^{(2)}$ [34]. The premise is that the short-distance pair correlations of the N -body cluster, if scaled by an overall factor, collapse approximately. Specifically, the dimensionless two-body contact $C_N^{(2)}$ of the N -atom cluster is found by enforcing [34,55–57]

$$P_N^{(2)}(r) \xrightarrow{\text{small } r} C_N^{(2)} P_2^{(2)}(r). \quad (12)$$

The operator $\hat{P}_N^{(2)}(r)$ defined in Eq. (11) differs by an overall factor from the operator employed in Ref. [34]. Correspondingly, we convert the results from Ref. [34] to our definition when comparing our two-body contacts with theirs. Equation (12) implies $C_N^{(2)} = 1$ for $N = 2$. In practice, $C_N^{(2)}$ is treated as a fit parameter when matching the left- and right-hand sides of Eq. (12), including only the short-distance region where $P_N^{(2)}(r)$ ($N > 2$) takes values between about 5% and 95–100% of its maximum. Reference [34] extracted the two-body contact for helium clusters interacting through the realistic LM2M2 potential [85], an interaction model that is similar to models IA, IB, and IC used in our work. Section III determines the two-body contact at the physical point for models IA, IB, and IC and, furthermore, discusses that the two-body contact has limited meaning for N -atom clusters interacting through model II. This is not unexpected since V_{int} for model II includes a three-body potential.

In addition to the pair distribution function, we monitor the probability $\rho^2 P_N^{(\text{jacobi})}(\rho)$ to find one of the particles located at a distance ρ from the center of mass of the other $N - 1$

particles. The corresponding operator is $\hat{P}_N^{(\text{jacobi})}(\rho)$,

$$\hat{P}_N^{(\text{jacobi})}(\rho) = \frac{1}{N} \sum_{j=1}^N \frac{\delta(\rho_j - \rho)}{\rho^2}, \quad (13)$$

where

$$\rho_j = \left| \vec{r}_j - \frac{1}{N-1} \sum_{k=1, k \neq j}^N \vec{r}_k \right|. \quad (14)$$

Since the lowest breakup threshold of the N -particle cluster corresponds to the breakup into a cluster consisting of $N-1$ atoms and a single far-separated atom, $\hat{P}_N^{(\text{jacobi})}(\rho)$ should—in the large- ρ limit—fall off as

$$P_N^{(\text{jacobi})}(\rho) \xrightarrow{\text{large } \rho} A_N \rho^{-2} \exp(-2\kappa_N \rho), \quad (15)$$

where the binding momentum κ_N is defined through $\sqrt{2\mu_N \epsilon_N}/\hbar$, the binding energy ϵ_N of the N -particle cluster is defined with respect to the ground-state energy E_{N-1} of the $N-1$ cluster, and μ_N is equal to $(N-1)m/N$. By comparing the tail of $P_N^{(\text{jacobi})}(\rho)$ with the expected asymptotic behavior, the extent of the universal, binding-energy-dominated regime can be determined. We note that $\lim_{r \rightarrow \infty} P_N^{(2)}(r)$ and $\lim_{\rho \rightarrow \infty} P_N^{(\text{jacobi})}(\rho)$ behave, except for an overall normalization constant, identically. For ground-state helium clusters with $N \geq 3$, the r region over which $P_N^{(2)}(r)$ is governed by the binding momentum is notably smaller than the ρ region over which $P_N^{(\text{jacobi})}(\rho)$ is governed by the binding momentum. This can be seen by rewriting ρ_j ,

$$\rho_j = \left| \frac{1}{N-1} \sum_{k=1, k \neq j}^N \vec{r}_{j,k} \right|. \quad (16)$$

For $\rho_j \rightarrow \infty$, the vectors $\vec{r}_{j,k}$ are all parallel and $P_N^{(\text{jacobi})}(\rho)$ and $P_N^{(2)}(r)$ agree, except for an overall normalization factor. When ρ_j is finite, the vectors $\vec{r}_{j,k}$ with $k=1, \dots, j-1, j+1, \dots, N$ are not all parallel and $P_N^{(2)}(r)$ deviates from $P_N^{(\text{jacobi})}(\rho)$.

To quantify the three-body correlations of the ${}^4\text{He}_N$ clusters, we monitor two complementary distribution functions, $P_N^{(3, \text{jacobi})}(\rho_3)$ and $P_N^{(3, \text{shape})}(\bar{x}, \bar{y})$. The three-body Jacobi distribution function $P_N^{(3, \text{jacobi})}(\rho_3)$, which is measured by the operator $\hat{P}_N^{(3, \text{jacobi})}(\rho_3)$, is

$$\begin{aligned} \hat{P}_N^{(3, \text{jacobi})}(\rho_3) &= \frac{2}{N(N-1)(N-2)} \sum_{j=1}^{N-2} \sum_{k>j}^{N-1} \sum_{l>k}^N \\ &\times \left[\frac{\delta(\rho_{jk,l} - \rho_3)}{(\rho_3)^2} + \frac{\delta(\rho_{jl,k} - \rho_3)}{(\rho_3)^2} \right. \\ &\left. + \frac{\delta(\rho_{kl,j} - \rho_3)}{(\rho_3)^2} \right], \end{aligned} \quad (17)$$

where

$$\rho_{jk,l} = \left| \vec{r}_l - \frac{1}{2}(\vec{r}_j + \vec{r}_k) \right|. \quad (18)$$

The quantity $(\rho_3)^2 P_N^{(3, \text{jacobi})}(\rho_3)$ tells us, for each triple within the N -body cluster, the likelihood to find one of the particles at

distance ρ_3 from the center of mass of the other two particles of the triple. In analogy to the two-body contact $C_N^{(2)}$, we define a $(2+1)$ or pair-atom contact $C_N^{(2+1)}$ for $N \geq 3$ through

$$P_N^{(3, \text{jacobi})}(\rho_3) \xrightarrow{\text{small } \rho_3} C_N^{(2+1)} P_3^{(3, \text{jacobi})}. \quad (19)$$

Equation (19) defines the pair-atom contact $C_N^{(2+1)}$ through the short-range behavior of the distribution function. Alternatively, we may define $C_N^{(2+1)}$ by assuming that the many-body wave function Ψ factorizes when $\rho_{jk,l}$ takes on small values,

$$\begin{aligned} \Psi(\vec{r}_1, \dots, \vec{r}_N) &\xrightarrow{\text{small } \rho_{jk,l}} \\ \Phi(\vec{\rho}_{jk,l}) B_N^{(2+1)}(\vec{r}_{j,k}, \vec{R}_{j,k,l}, \{\vec{r}_{n;n \neq j,k,l}\}), \end{aligned} \quad (20)$$

where $\vec{R}_{j,k,l} = (\vec{r}_j + \vec{r}_k + \vec{r}_l)/3$. The function $B_N^{(2+1)}$ is nonuniversal and the limit in Eq. (20) is taken while keeping $\vec{r}_{j,k}$, $\vec{R}_{j,k,l}$, and all $\{\vec{r}_{n;n \neq j,k,l}\}$ unchanged. If the pair-atom function $\Phi(\vec{\rho}_{jk,l})$ is universal, then the pair-atom contact is a meaningful quantity and can be related to $\Phi(\vec{\rho}_{jk,l})$ following the same steps as when relating the two-body contact, the relevant product ansatz, and the pair distribution function (see, e.g., Ref. [34]). While the $(2+1)$ contact characterizes three-body correlations of N -particle systems, it differs conceptually from the three-body contact considered in the literature [59,60].

Since the distribution function $P_N^{(3, \text{jacobi})}(\rho_3)$ does not capture the relative orientation of the subtrimers (the angles are being averaged over), we additionally monitor the normalized trimer correlation function $P_N^{(3, \text{shape})}(\bar{x}, \bar{y})$, which captures the relative orientation of any three atoms within the N -atom cluster [26]. For each triple spanned by \vec{r}_j , \vec{r}_k , and \vec{r}_l , we determine the maximum of $r_{j,k}$, $r_{j,l}$, and $r_{k,l}$ and scale all lengths by this value. For concreteness, let us assume that $r_{j,k}$ is larger than $r_{j,l}$ and $r_{k,l}$. Next, we rotate the triangle spanned by \vec{r}_j , \vec{r}_k , and \vec{r}_l so that it lies in the xy plane, so that the normalized position vectors of particles j and k are equal to $(x, y, z) = (\pm 1/2, 0, 0)$, and so that the y coordinate of particle l is positive. The distribution $P_N^{(3, \text{shape})}(\bar{x}, \bar{y})$ yields the likelihood that the l th particle has the normalized, rotated position vector $(\bar{x}, \bar{y}, 0)$.

The hyper-radial distribution function $P_N^{(\text{hyper})}(\rho_N)$ is measured by the operator $\hat{P}_N^{(\text{hyper})}(\rho_N)$,

$$\hat{P}_N^{(\text{hyper})}(\rho_N) = \frac{\delta(\rho_N - R)}{R^{3N-4}}, \quad (21)$$

where R is the hyper-radius,

$$R^2 = \frac{1}{N^2} \sum_{j=1}^{N-1} \sum_{k>j}^N r_{j,k}^2. \quad (22)$$

The normalization is such that

$$\int_0^\infty P_N^{(\text{hyper})}(\rho_N) (\rho_N)^{3N-4} d\rho_N = 1. \quad (23)$$

The quantity $(\rho_N)^{3N-4} P_N^{(\text{hyper})}(\rho_N)$ tells one the likelihood that the N -atom cluster has the hyper-radius ρ_N . The hyper-radius provides a measure of the cluster size [32,86,87]. Our definition of the hyper-radius implies a hyper-radial mass of M ,

$$M = Nm. \quad (24)$$

Section III uses the hyper-radial distribution functions to determine approximate effective hyper-radial potential curves assuming separability of the hyper-radial and hyperangular degrees of freedom. Despite the crudeness of the approach (the coupling of the hyper-radial and hyperangular degrees of freedom can, in general, not be neglected), the resulting approximate hyper-radial potential curves provide, as shown in Sec. III, some insight.

The kinetic energy release (KER),

$$\text{KER} = \sum_{j=1}^{N-1} \sum_{k>j}^N \frac{1}{r_{j,k}}, \quad (25)$$

of the helium dimer as well as pure and mixed-isotope helium trimers has been measured in Coulomb explosion experiments [26,36,88]. While it is not clear that the experimental determination of the KER generalizes straightforwardly to larger clusters [89,90], Sec. III reports and interprets the KER for helium clusters with up to $N = 10$ particles.

III. RESULTS

This section presents results for the observables defined in Sec. II C. In addition to tracking the structural properties as a function of N , particular focus is placed on comparing

(i) the characteristics of helium clusters at the physical point (“true” helium clusters) and quantum clusters at unitarity (helium-helium interaction artificially tuned to unitarity);

(ii) the characteristics of helium clusters at the physical point interacting through the three realistic interaction potentials model IA, model IB, and model IC;

(iii) the characteristics of helium clusters at the physical point interacting through the realistic HFD-HE2 potential (model IA) and the effective low-energy potential (model II); and

(iv) the characteristics of helium clusters at unitarity interacting through the realistic HFD-HE2 potential and the effective low-energy potential.

To put the structural properties into context, we discuss a few characteristics of the energies at the physical point (see Table I) and at unitarity (see Table II). Table I shows that the two-body binding energy for the CPKMJS potential at the physical point is 1.95 times larger than that for the HFD-HE2 potential. For $N = 3$, the difference in the energy is notably smaller, namely, the energy for the CPKMJS potential at the physical point is 12% larger than that for the HFD-HE2 potential. As N increases, the difference decreases from 8% for $N = 4$ to 4% for $N = 10$. For $N = 10$, this percentage difference between the energy for model IB and model IA is similar to that between the energy for the effective low-energy model II and model IA. Table II shows that the dependence of the energy at unitarity is, for the scaled realistic interaction potentials, notably suppressed compared to the physical point. Specifically, the energies for $N = 3$ –10 for the CPKMJS potential are slightly larger than those for the HFD-HE2 potential (rounding, the percentage is 100%).

The solid lines in Fig. 1 show the likelihood $\rho^2 P_N^{(\text{jacobi})}(\rho)$ for realistic interaction models to find a particle at distance ρ from the center of mass of the other $N - 1$ particles for

$N = 3$ –10. The color of the lines changes nearly continuously from green for $N = 3$ to dark red for $N = 10$. The top and bottom rows show results at the physical point and at unitarity, respectively. It can be seen that the distributions at unitarity extend to somewhat larger ρ , owing to the smaller binding energies ϵ_N at unitarity than at the physical point. The third column compares results for the HFD-HE2 potential and the effective low-energy model. It can be seen that the large- ρ behavior of $\rho^2 P_N^{(\text{jacobi})}(\rho)$ for the HFD-HE2 potential (model IA, solid lines) and for the effective low-energy potential (model II, dotted lines) agrees well. This is expected since the effective low-energy potential has been shown to reproduce the energies of the N -particle cluster interacting through the HFD-HE2 potential at the 95% or higher level (see Ref. [33] and Tables I and II).

The solid lines in the left and middle columns of Fig. 1 show $\rho^2 P_N^{(\text{jacobi})}(\rho)$ for the realistic CPKMJS potential (model IB) on a linear and logarithmic scale, respectively. The logarithmic representation allows us to visually quantify the portion of the distribution that is governed by the exponential binding momentum dominated fall-off. Specifically, the dotted lines show the expected fall-off, using the binding momentum κ_N , obtained by combining DMC energies of clusters containing N and $N - 1$ atoms, as input. To plot the dotted lines, the normalization constant A_N , given by Eq. (15), is treated as a fitting parameter to best match the large- ρ tail, including $\rho \geq \rho_m$, where ρ_m is adjusted such that $\int_{\rho_m}^{\infty} P_N^{(\text{jacobi})}(\rho) \rho^2 d\rho$ is equal to 0.2. The visual agreement at large ρ between the solid and dotted lines in the middle column of Fig. 1 is good.

Figure 2 shows the scaled pair distribution functions $r^2 P_N^{(2)}(r)$ for $N = 2$ –10 at the physical point (top row) and at unitarity (bottom row). The scaled pair distribution functions for the realistic interaction models display a clear maximum for $N \lesssim 6$. For larger N , the maximum broadens and shifts to larger r values; for these larger N , the scaled pair distribution functions display a hint of a double-peak structure that can be interpreted as a signature of the development of a “second length scale or shell.” It is important to keep in mind that the clusters at the physical point and at unitarity are extremely floppy and diffuse and that the terms “second length scale” and “second shell” should be contextualized within the framework of extremely diffuse quantum liquids. The double-peak structure is not reproduced by the low-energy model (dotted lines in the third column).

The third column of Fig. 2 shows that the quantities $r^2 P_N^{(2)}(r)$ for model IA (solid lines) and model II (dotted lines) differ for small r ($r \lesssim 20 a_0$). Interestingly, the scaled pair distribution functions for the HFD-HE2 potential and the CPKMJS potential (solid lines) rise at about the same r value for all N , namely, at $r \approx 4.5 a_0$ or $r \approx 0.9 r_{\text{vdW}}$. Careful inspection shows that the rise is shifted to somewhat larger r values for the clusters at unitarity interacting through realistic potentials than for the clusters at the physical point interacting through realistic potentials. The scaled pair distribution functions for the effective low-energy potential (model II, dotted lines), in contrast, rise at much smaller r values. The scaled pair distribution functions for model I and model II are different at small r for two reasons: (i) The two-body

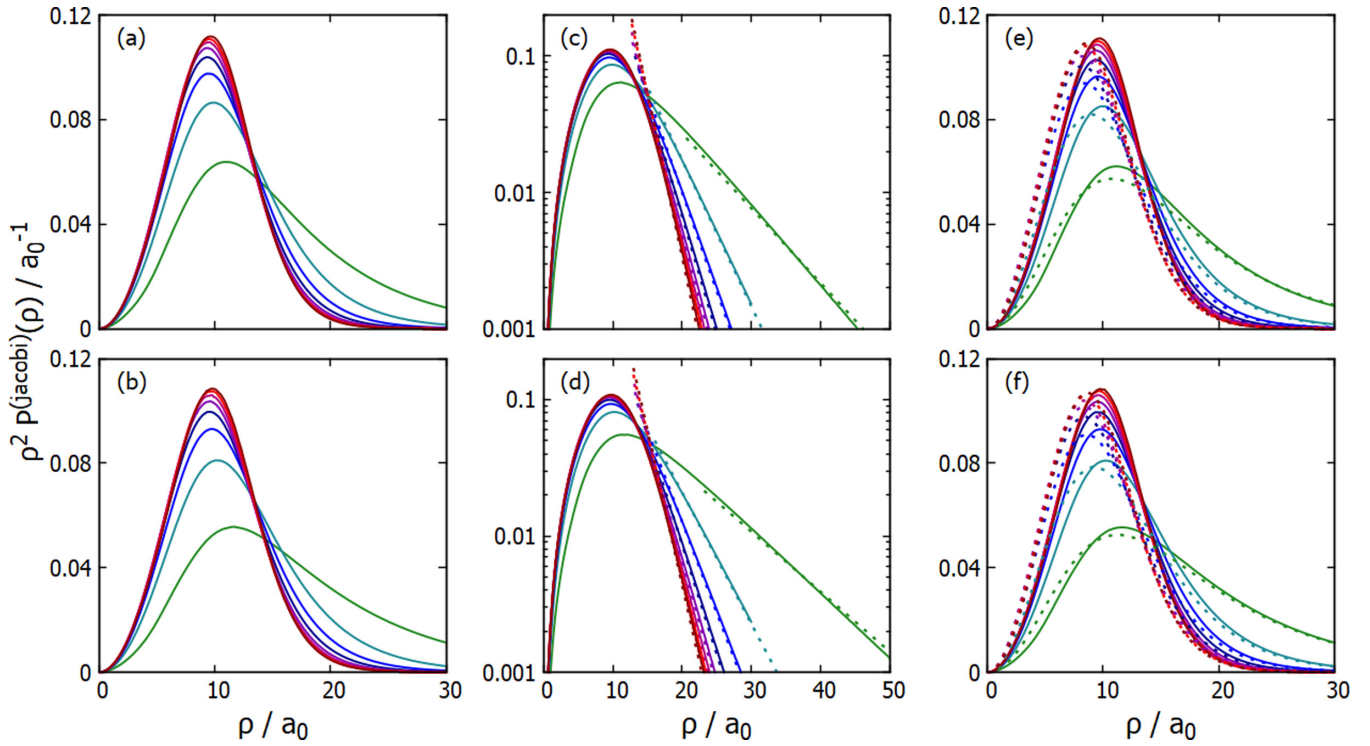


FIG. 1. $\rho^2 P_N^{(\text{jacob})}(\rho)$ for $N = 3$ – 10 at the physical point (top row) and at unitarity (bottom row). The solid lines in (a)–(d) show $\rho^2 P_N^{(\text{jacob})}(\rho)$ for model IB. At $\rho = 20 a_0$, the curves are ordered, from top to bottom, from the smallest N (the curve for $N = 3$ is green) to the largest N (the curve for $N = 10$ is dark red). Note that the data shown in the first and second columns are identical, but that the x and y scales differ. The dotted lines in (b) and (d) show the asymptotic behavior $A_N \exp(-2\kappa_N \rho)$, using the numerically determined binding momentum κ_N and treating the “normalization constant” A_N as a fitting parameter. The solid and dotted lines in (e) and (f) (third column) show $\rho^2 P_N^{(\text{jacob})}(\rho)$ for model IA and model II, respectively. The agreement between the dotted and solid lines is excellent at large ρ and deteriorates for smaller ρ . The deterioration is due to the inability of the low-energy model to fully capture the small length scale correlations. The color scheme used here is also used in Figs. 2, 3, 4(a), 6, and 7, and in the Supplemental Material [82], Figs. S3 and S4. The layout used here, i.e., the top row showing results at the physical point and the bottom row showing results at unitarity, is also used in Figs. 2, 5–7, and in the Supplemental Material [82], Fig. S4.

Gaussian potential used in model II does not have a hard wall at small r . (ii) Model II contains a repulsive three-body Gaussian potential, which alters the behavior when three particles are in close vicinity to each other, impacting the short-distance correlations of two-, three-, and higher-body subclusters.

To highlight the universality of the short-range behavior of the scaled pair distribution function $r^2 P_N^{(2)}(r)$ for realistic interaction models, Fig. 3 replots $r^2 P_N^{(2)}(r)$ at the physical point—including the factor $C_N^{(2)}$ —for model IA (dash-dotted lines) and model IB (solid lines). As discussed in Sec. II, the two-body contact $C_N^{(2)}$ is determined by fitting the $N > 2$ curves for small r to the $N = 2$ curve. It can be seen that the rise of the scaled curves collapses for $N = 2$ – 10 in the regime $r \lesssim 1.4 r_{\text{vdW}}$ separately for both interaction models. The fact that the curves for each of the interaction models collapse confirms that the two-body contact $C_N^{(2)}$, determined in the manner described in Sec. II, provides a meaningful characterization of the short-distance behavior of van der Waals clusters.

Table S3 (see Supplemental Material [82]) reports $C_N^{(2)}$ for helium clusters with $N = 3$ – 10 interacting through models IA–IC at the physical point. The ratio of $C_N^{(2)}$, $N \geq 3$, for two different interaction potentials is approximately constant. To leading order, this ratio is given by the ratio of a_s/r_{vdW}

for the two different interaction potentials. Specifically, the values for the HFD-HE2 potential are between 1.32 and 1.38 times larger than those for the CPKMJS potential; for comparison, $(a_s/r_{\text{vdW}})_{\text{HFD-HE2}}/(a_s/r_{\text{vdW}})_{\text{CPKMJS}}$ is equal to 1.40. Those for the TTY potential are between 1.09 and 1.10 times larger than those for the CPKMJS potential; for comparison, $(a_s/r_{\text{vdW}})_{\text{TTY}}/(a_s/r_{\text{vdW}})_{\text{CPKMJS}}$ is equal to 1.10.

To understand this behavior, we recall that the pair distribution functions for the realistic interaction potentials at the physical point are, for $N \gtrsim 5$, to a very good approximation independent of the potential model [compare, e.g., the solid lines in Figs. 2(a) and 2(e)]. The $N = 2$ pair distribution functions, in contrast, differ notably. Because of this, the difference between the contacts $C_N^{(2)}$, $N \gtrsim 5$, for model IA and model IB predominantly reflects the difference between the respective $N = 2$ pair distribution functions. Specifically, using the fact that the dimers are weakly bound and the pair distribution functions are normalized, the difference in the height of $r^2 P_2^{(2)}(r)$ at small r for different realistic potential models can be expressed in terms of the binding momentum and thus, using effective range theory, in terms of a_s/r_{vdW} . Assuming that the pair distribution functions for different potential models agree for larger N , we find that the ratio of the two-body contacts for larger N is given, to leading order,

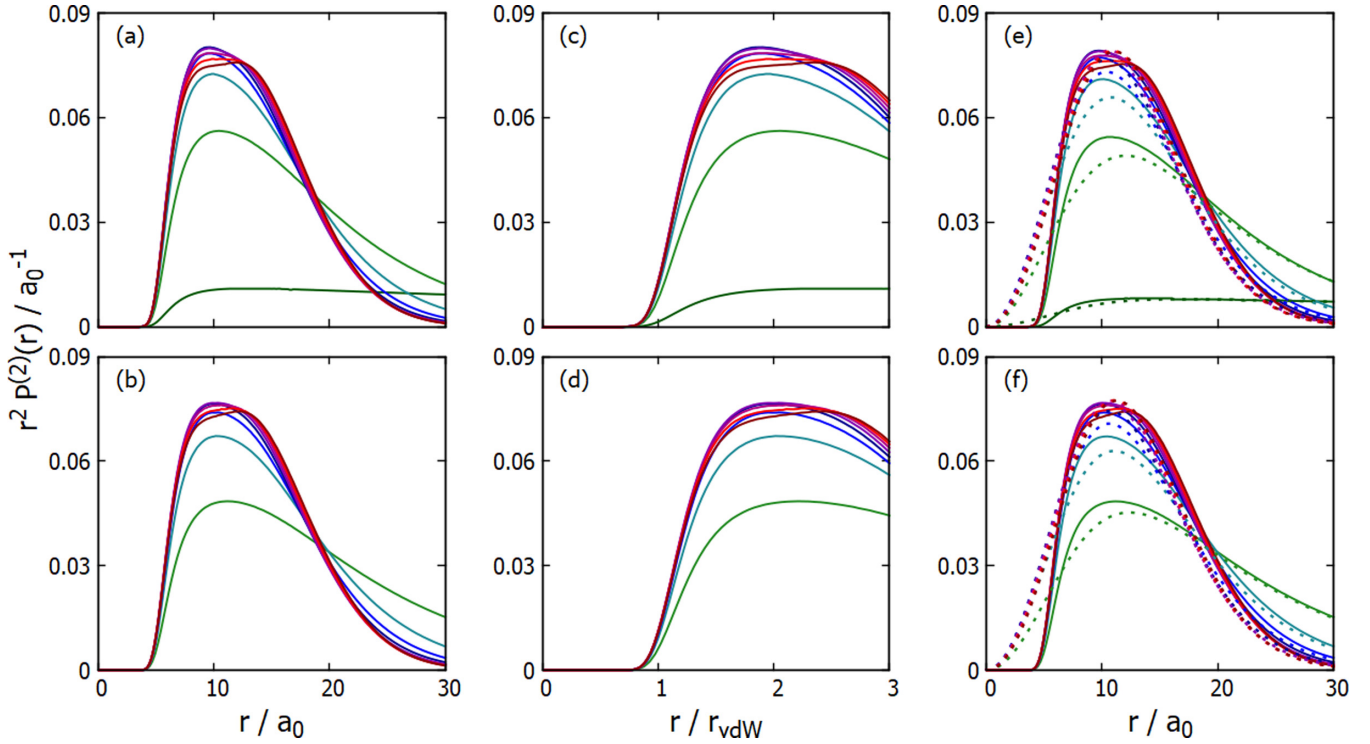


FIG. 2. $r^2 P_N^{(2)}(r)$ for $N = 2-10$ at the physical point (top row) and for $N = 3-10$ at unitarity (bottom row). The solid lines in (a)–(d) show $r^2 P_N^{(2)}(r)$ for model IB. Note that the data shown in the first and second columns are identical: the first column shows r in units of a_0 and the second column shows r in units of r_{vdW} , focusing on the small- r region. It can be seen that the scaled pair distribution functions for different N collapse approximately for $r \approx r_{\text{vdW}}$. The solid and dotted lines in (e) and (f) (third column) show $r^2 P_N^{(2)}(r)$ for model IA and model II, respectively. Differences are most pronounced in the $r \lesssim 20 a_0$ region. The color scheme is the same as in Fig. 1.

by the ratio between a_s/r_{vdW} for the two interaction potentials. Our analysis indicates that the N dependence of the two-body contact $C_N^{(2)}$ for helium clusters at the physical point interacting through one realistic interaction model is, to a fairly good approximation, universally linked to that for helium clusters interacting through another realistic interaction model. The arguments presented here are reminiscent of the discussion of effective range corrections to the asymptotic normalization constant, which is defined by relating the “true” nuclear wave function to a wave function that is calculated assuming that the effective interaction in the asymptotically dominant channel has vanishing range [91,92].

Table S3 (see Supplemental Material [82]) also compares our results with those obtained in Ref. [34] for the LM2M2 potential. The $C_N^{(2)}$ values for the LM2M2 potential are between 1.06 and 1.08 times larger than those for the CPKMJS potential; this is quite a bit smaller than $(a_s/r_{\text{vdW}})_{\text{LM2M2}}/(a_s/r_{\text{vdW}})_{\text{CPKMJS}} = 1.13$. We expect that the LM2M2 data from Ref. [34] would follow the same trends as displayed by our data; we speculate that the differences might be related to the different data analysis strategies employed.

Last, we note that our analysis of the short-distance behavior of the scaled pair distribution functions for the effective low-energy model II reveals that the small- r behaviors of $r^2 P_2^{(2)}(r)$ and $r^2 P_N^{(2)}(r)$ with $N \geq 3$ do not collapse as neatly by introducing an r -independent scaling factor for each N (see Fig. S3 from the Supplemental Material [82]) as the corresponding data for the realistic interaction models. Due to the presence of the repulsive three-body potential, the low-energy

model does not capture the small- r , “high-energy” van der Waals universality of the pair distribution function.

The fact that the curves for model IA in Fig. 3 are pushed to larger r compared to those for model IB can be interpreted as being due to model IA being characterized by a larger effective repulsion than model IB: the two-body s -wave scattering length for model IA is larger than that for model IB ($a_s = 234.84 a_0$ compared to $a_s = 170.86 a_0$). Interestingly, the rise of the scaled pair distribution functions is captured quantitatively by the universal van der Waals function $\varphi_{\text{vdW}}(r)$ [93,94],

$$\varphi_{\text{vdW}}(r) = B[\Gamma(5/4)x^{1/2}J_{1/4}(2x^{-2}) - \frac{r_{\text{vdW}}}{a_s}\Gamma(3/4)x^{1/2}J_{-1/4}(2x^{-2})], \quad (26)$$

which is obtained by solving the scaled radial Schrödinger equation for a purely attractive $-C_6/r^6$ potential. In Eq. (26), x is equal to r/r_{vdW} . Thin black dash-dotted and solid lines in Fig. 3 show the quantity $|\varphi_{\text{vdW}}(r)|^2$ for model IA ($a_s/r_{\text{vdW}} = 46.95$) and model IB ($a_s/r_{\text{vdW}} = 33.63$), respectively. The nodes of the wave function $\varphi_{\text{vdW}}(r)$ in the $r \lesssim r_{\text{vdW}}$ region reflect the presence of deep-lying two-body bound states. For r values beyond the last node, the density $|\varphi_{\text{vdW}}(r)|^2$ agrees well with $r^2 P_2^{(2)}(r)/C_N^{(2)}$. For the infinite scattering length case, Refs. [53,54] established the van der Waals universality of the short-distance correlations of the scaled pair distribution function of trimers interacting through realistic interaction

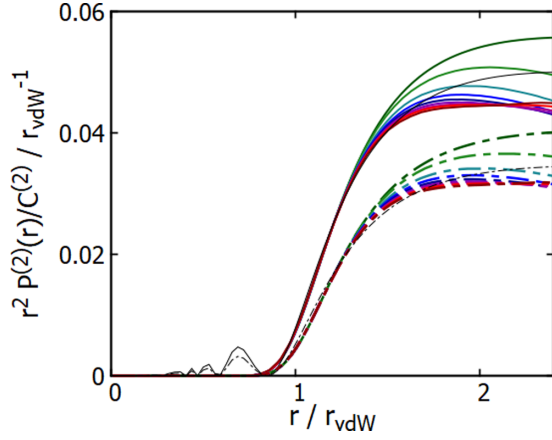


FIG. 3. $r^2 P_N^{(2)}(r)/C_N^{(2)}$, $N = 2-10$, for two realistic interaction potentials at the physical point. The sets of dash-dotted and solid lines show results for model IA and model IB, respectively. The color scheme is the same as in Fig. 1. The thin black dash-dotted and solid lines show the universal van der Waals function $|\varphi_{\text{vdW}}(r)|^2$, given by Eq. (26), for model IA and model IB, respectively (these two models are characterized by slightly different r_{vdW}); the normalization constant B is adjusted by fitting $|\varphi_{\text{vdW}}(r)|^2$ to $r^2 P_2^{(2)}(r)$, including r values ($r \lesssim 2r_{\text{vdW}}$) for which $P_2^{(2)}(r)$ takes values that are larger than 5% and smaller than the maximum of $P_2^{(2)}(r)$ for model IA and smaller than 95% of the maximum of $P_2^{(2)}(r)$ for model IB, respectively.

potentials. Figure 3 shows that $|\varphi_{\text{vdW}}(r)|^2$ captures the short-distance correlations of $r^2 P_N^{(2)}(r)$ also for helium clusters at the physical point.

Figures 4 and 5 as well as Fig. S4 in the Supplemental Material [82] summarize the three-body correlations of N -atom clusters. Figure S4 [82], which shows the quantity $(\rho_3)^2 P_N^{(3,\text{jacobi})}(\rho_3)$, highlights two key points. First, the scaled three-body distributions $(\rho_3)^2 P_N^{(3,\text{jacobi})}(\rho_3)$ for model IB and model II (first and third columns) are visually indistinguishable, including in the small- ρ_3 region; this is in clear contrast to the behavior of the scaled pair distribution functions. Second, the quantity $(\rho_3)^2 P_N^{(3,\text{jacobi})}(\rho_3)$ becomes narrower as N changes from $N = 3$ to $N = 4$ to $N = 5$, but changes comparatively little for $N = 6-10$. This indicates that the correlations of the three-body subsystem saturate approximately for these N values. This ‘‘saturation’’ is different from the behavior of the scaled pair distribution functions, which show a more pronounced N dependence for $N = 6-10$.

Figure 4(a) focuses on the small- ρ_3 behavior at the physical point. The solid and dash-dotted lines show $[(\rho_3)^2 P_N^{(3,\text{jacobi})}(\rho_3)/C_N^{(2+1)}]/r_{\text{vdW}}^{-1}$ for $N = 3-10$ for model IA and model II, respectively; to make the figure, the x and y axes are scaled using the van der Waals length r_{vdW} for the HFD-HE2 potential (model IA). The collapse of the scaled distribution functions is extremely clean for the realistic interaction potential (solid lines) and very clean for the low-energy potential (dash-dotted lines). Differences between the scaled curves for the realistic and low-energy models are clearly visible for small ρ_3 . Figures 4(b) and 4(c) show the N dependence of the $(2+1)$ contact $C_N^{(2+1)}$ at the physical point and

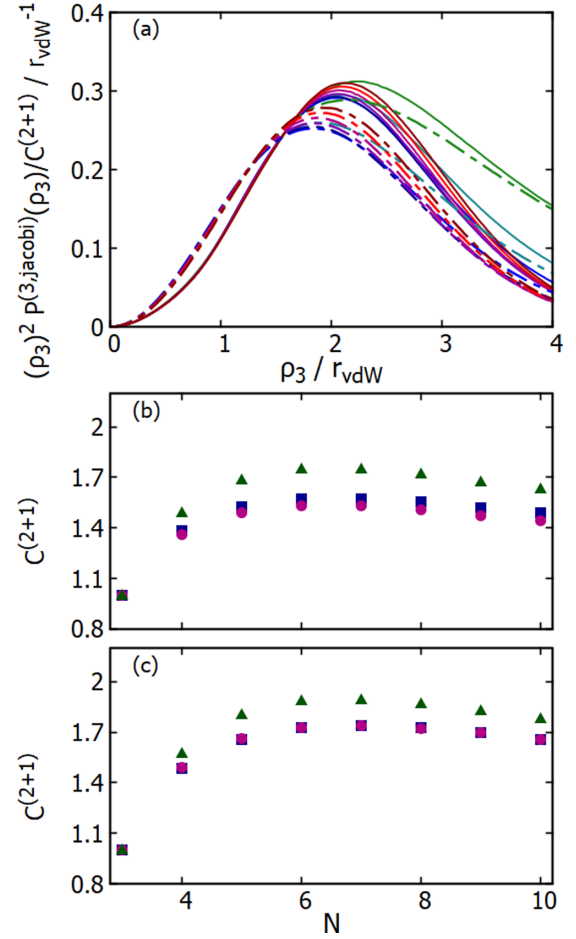


FIG. 4. Triple correlations and $(2+1)$ contact. (a) The solid and dash-dotted lines show $(\rho_3)^2 P_N^{(3,\text{jacobi})}(\rho_3)/C_N^{(2+1)}$ for the realistic HFD-HE2 potential (model IA) and the effective low-energy potential (model II), respectively, at the physical point for $N = 3-10$. The color scheme is the same as in Fig. 1. (b) The squares, circles, and triangles show the pair contact $C_N^{(2+1)}$ at the physical point as a function of N for models IA, IB, and II, respectively. (c) The squares, circles, and triangles show the pair contact $C_N^{(2+1)}$ at unitarity as a function of N for models IA, IB, and II, respectively.

at unitarity, respectively, for three different interaction potentials. The overall trends are the same for all three interaction potentials: $C_N^{(2+1)}$ increases for $N \lesssim 6$ or 7 and then slowly decreases. The contacts $C_N^{(2+1)}$ for the low-energy model (triangles) are notably larger for $N \geq 4$ than those for the realistic potentials (squares and circles). Interestingly, while the contacts $C_N^{(2+1)}$ for the two realistic potentials (model IA and model IB) differ by a small amount for $N \geq 4$ at the physical point, they coincide, within our numerical accuracy, at unitarity (see numerical values of $C_N^{(2+1)}$ collected in Table S4 of the Supplemental Material [82]). This behavior of the contact is related to the three-body energies. The ratio $E_{\text{CPKMS}}/E_{\text{HFD-HE2}}$ is equal to 1.12 at the physical point (see Table I) and 1.00 at unitarity (see Table II).

As already mentioned in Sec. II, the $(2+1)$ contact investigated here differs from the three-body contact investigated in Refs. [59,60] at the physical point. While the three-body contact for realistic interaction models is, to a large degree,

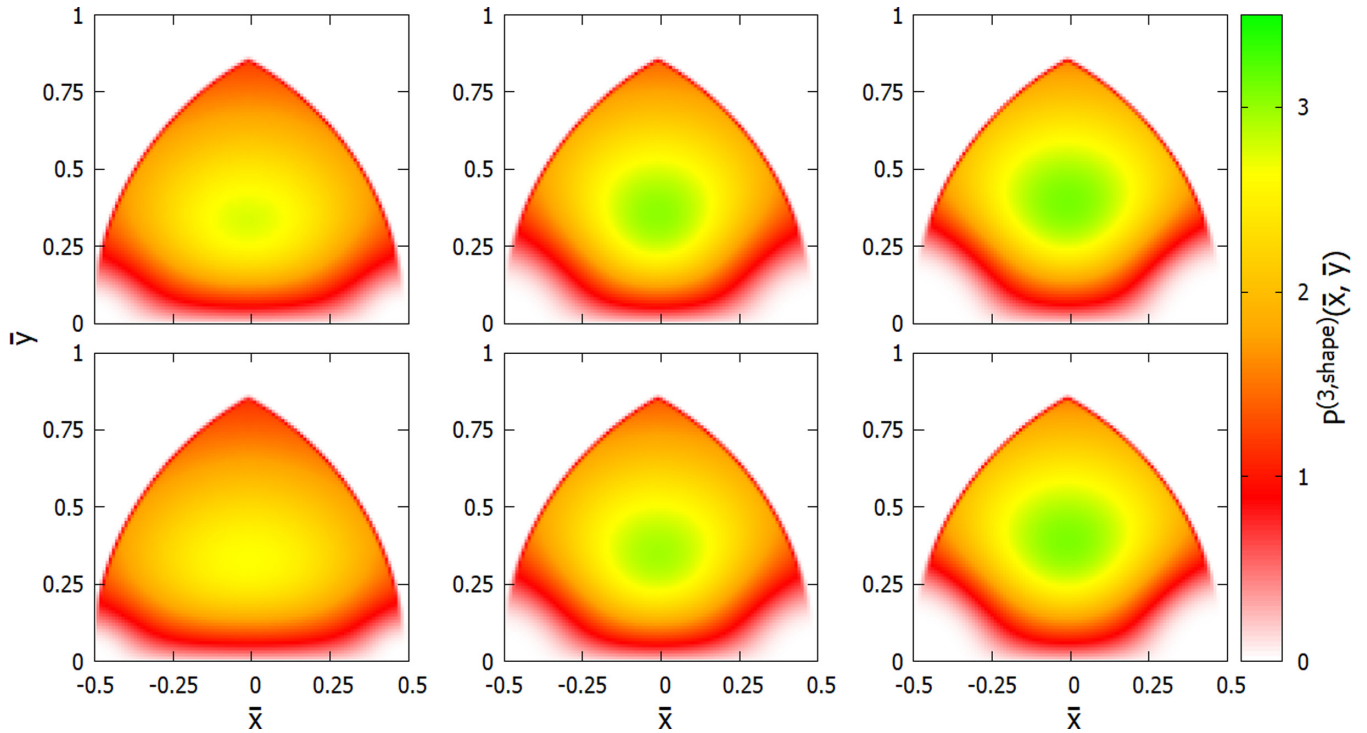


FIG. 5. $P_N^{(3,\text{shape})}(\bar{x}, \bar{y})$ for model IB at the physical point (top row) and at unitarity (bottom row). The first, second, and third columns show results for $N = 3$, $N = 4$, and $N = 10$, respectively. The color bar on the right applies to all six panels. Since the triangles are oriented and normalized such that one particle sits at $(\bar{x}, \bar{y}) = (-1/2, 0)$ and the other at $(\bar{x}, \bar{y}) = (+1/2, 0)$ (with the interparticle distance vector corresponding to the largest distance being oriented along the $\pm\bar{x}$ axis), the regions in the top left and top right of the panels are excluded by construction.

governed by the short-distance two-body correlations, the three-body contact for the low-energy model depends notably on the repulsive three-body potential. The $(2 + 1)$ contact, in contrast, captures the behavior as a third particle approaches the center of mass of a two-body subunit of any size. As such, the $(2 + 1)$ contact probes, on average, larger length scales than the three-body contact. Correspondingly, the low-energy model does a better job of reproducing the $(2 + 1)$ contact obtained for the realistic potentials than it does of reproducing the three-body contact obtained for the realistic potentials (we are not showing data for the three-body contact).

To gain insights into the distribution of the shapes that the triples are arranged in, the first, second, and third columns of Fig. 5 show the distribution function $P_N^{(3,\text{shape})}(\bar{x}, \bar{y})$ for $N = 3$, $N = 4$, and $N = 10$, respectively. We observe that the distributions, and thus the structures, at the physical point (top row) and at unitarity (bottom row) are very similar. The highest probability is found at $\bar{x} = 0$ and $\bar{y} \approx 0.35$, which corresponds to a slightly elongated triangle. Even though the distributions have a maximum, the clusters' wave functions include essentially all shapes, except for those where two particles sit on top of each other ($\bar{y} = 0$ and arbitrary \bar{x}) and where the triangles are highly elongated ($\bar{y} \approx 0$ and $\bar{x} \approx \pm 0.5$). Figure 5 shows that the distributions become more peaked with increasing N and that the likelihood to find highly elongated triangles becomes smaller with increasing N .

Figures 6(a) and 6(b) show the scaled hyper-radial density $(\rho_N)^{3N-4} P_N^{(\text{hyper})}(\rho_N)$ for $N = 3$ –10 clusters interacting

through the CPKMJS potential at the physical point and at unitarity, respectively. The differences between the scaled hyper-radial densities at the physical point and at unitarity for fixed N are small. Careful inspection shows that the scaled hyper-radial densities at unitarity extend to larger ρ_N and rise at slightly larger ρ_N than those at the physical point. Correspondingly, the maximum of $(\rho_N)^{3N-4} P_N^{(\text{hyper})}(\rho_N)$ is located at slightly larger ρ_N for the clusters at unitarity than for the clusters at the physical point. The fact that the scaled hyper-radial densities at unitarity extend to larger ρ_N than those at the physical point is a consequence of the smaller binding energy at unitarity than at the physical point. As N increases, the scaled hyper-radial densities become more localized, with their maximum shifting to larger ρ_N . To interpret this behavior, one needs to keep in mind that the definition of the hyper-radius is intimately linked to the definition of the hyper-radial mass M . Since the quantity $M\rho_N^2$ is an invariant but not ρ_N and M separately, ρ_N can be multiplied by an overall factor [32,86,87]. If all interparticle distances were equal to \bar{r} , then ρ_N [as defined in Eq. (22)] would approach $\bar{r}/\sqrt{2}$ in the $N \rightarrow \infty$ limit. Since helium clusters behave roughly as incompressible liquids, the maximum of the hyper-radial density is expected to occur at increasingly larger ρ_N as N increases. Figures 6(a) and 6(b) confirm this notion.

We now use the hyper-radial densities to calculate approximate hyper-radial potential curves. We note that Ref. [32] obtained the effective hyper-radial potential curves of helium clusters with $N = 3$ –10 at the physical point following an

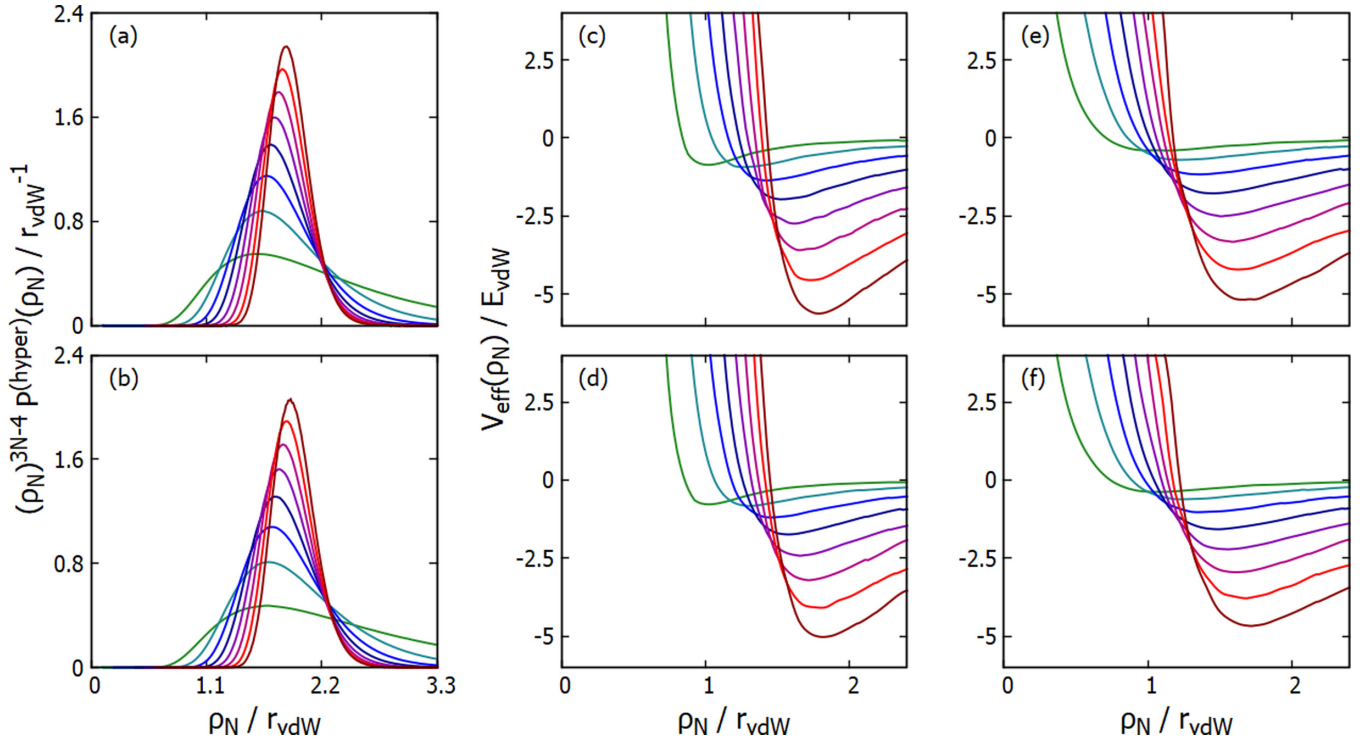


FIG. 6. Hyper-radial properties for $N = 3$ – 10 at the physical point (top row) and at unitarity (bottom row). The first column shows $P_N^{(\text{hyper})}(\rho_N)$ for model IA. The second column shows the (approximate) effective potential curves $V_{\text{eff}}(\rho_N)$ for model IA, calculated using Eq. (27). For comparison, the third column shows $V_{\text{eff}}(\rho_N)$ for model II (the model II plots are made using the van der Waals length for model IA as a scale). The color scheme is the same as in Fig. 1.

alternative and more rigorous approach; in addition, Ref. [32] presented careful benchmark calculations of the different approaches for $N = 3$. The approach pursued here yields potential curves that agree semiquantitatively with the more accurate potential curves presented in Ref. [32]. If the hyper-radial and hyperangular degrees of freedom separate, the effective one-dimensional Schrödinger equation for the lowest effective hyper-radial potential curve $V_{\text{eff}}(\rho_N)$ can be written in terms of $F_N(\rho_N)$ [59,95–98],

$$\left[-\frac{\hbar^2}{2M} \frac{\partial^2}{\partial \rho_N^2} + V_{\text{eff}}(\rho_N) \right] F_N(\rho_N) = E_N F_N(\rho_N), \quad (27)$$

where $F_N(\rho_N) = [(\rho_N)^{3N-4} P_N^{(\text{hyper})}(\rho_N)]^{1/2}$. For the N -particle clusters ($N \geq 3$) at unitarity, the separability is broken due to the finite-range nature of the two-body interactions. At the physical point, the finiteness of the scattering length provides an additional separability-breaking mechanism. Even though Eq. (27) is not strictly valid for the potential models considered in this work, we “invert” it to obtain approximate effective hyper-radial potentials $V_{\text{eff}}(\rho_N)$. The same strategy was pursued in Ref. [98] for $N = 3$ and 4. Figures 6(c) and 6(d) show the results for model IB at the physical point and at unitarity, respectively. The differences between the potential curves at the physical point and at unitarity are very small. Reference [98] conjectured, based on results for $N = 3$ and $N = 4$, that the location of the repulsive inner wall of the hyper-radial potential curves varies as $(N-1)r_{\text{vdW}}/\sqrt{2N}$; this scaling accounts for an effective nontrivial reduction of the configuration space due to an energy cost associated with

adiabatic deformation [53,54]. This scaling was contrasted with an alternative scaling of $\sqrt{N-1}r_{\text{vdW}}/\sqrt{2N}$, which arises assuming that the minimum average interparticle spacing is given by r_{vdW} . For $N = 10$, the inner wall would be located, according to these two scalings, at $0.671r_{\text{vdW}}$ and $2.01r_{\text{vdW}}$. Figures 6(c) and 6(d) show that the scaling is somewhere in between.

The corresponding effective hyper-radial potential curves for model II are shown in Figs. 6(e) and 6(f). The effective potential curves for model II are significantly softer (less steep) at small ρ_N (ρ_N/r_{vdW} between about 0.6 and 1.2) than those for model IB; this is consistent with what was discussed above for the pair distribution functions.

Last, Fig. 7 presents the KER distribution functions at the physical point (top row) and at unitarity (bottom row). While small helium clusters have been isolated in molecular beam experiments [26,88], Coulomb explosion experiments for $N \gtrsim 4$ are expected to be complicated by the fact the ions leaving the helium clusters might be undergoing additional collisions [89,90]. Despite this challenge, we find it useful to analyze the dependence of the KER distribution functions on the various interaction models. Since the number of interparticle distances increases as N^2 with increasing N , the KER distribution functions move to larger KER with increasing N . The KER distribution functions for model IA (first column) and model IB (second column) are nearly indistinguishable on the scale shown. Careful inspection reveals small differences between the KER distribution functions of clusters interacting through realistic interaction potentials at the physical point and at unitarity.

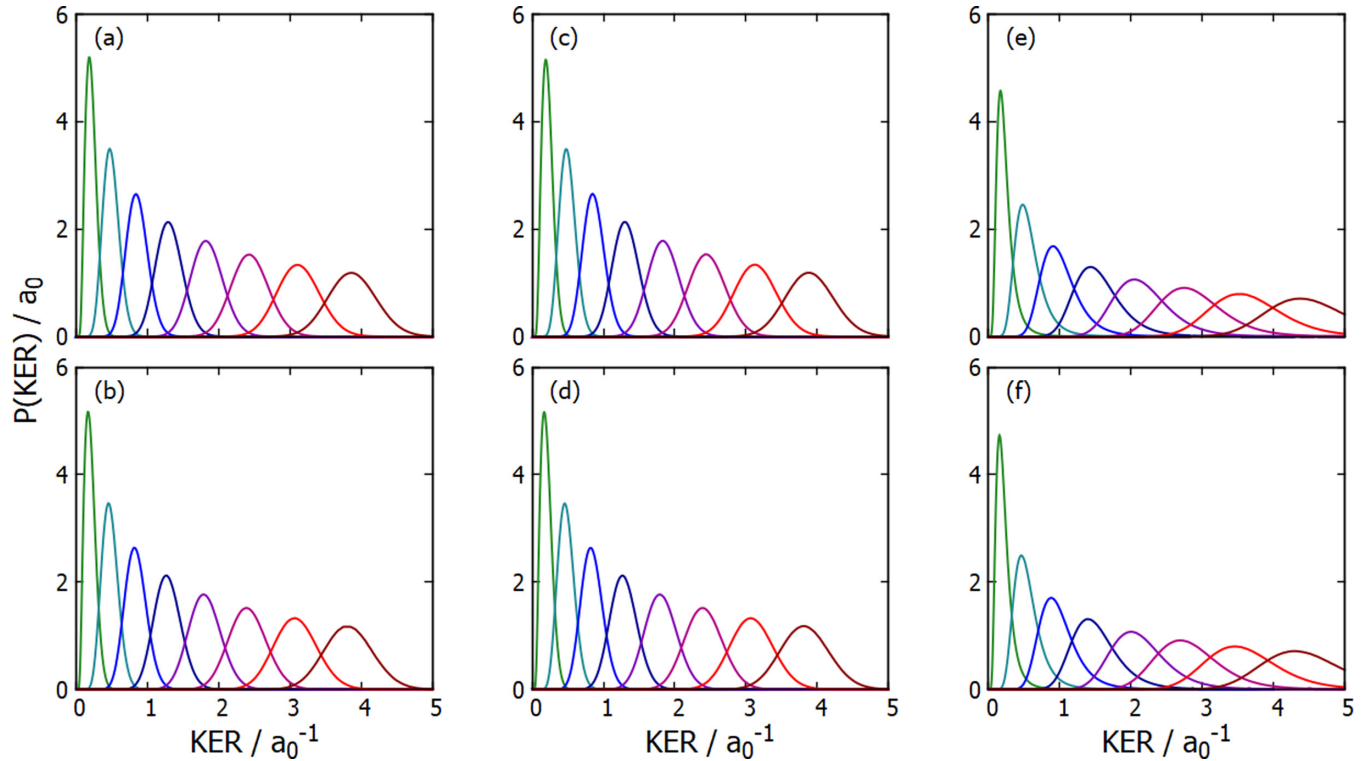


FIG. 7. KER for $N = 3-10$ at the physical point (top row) and at unitarity (bottom row). The first, second, and third columns show the KER for models IA, IB, and II, respectively. The color scheme is the same as in Fig. 1.

The KER distribution functions for clusters interacting through model II extend to significantly larger KER; this behavior is linked to the enhanced probability for clusters interacting through model II, relative to those interacting through realistic interaction potentials (model I), to find two particles at small interparticle distances. The broader KER distribution functions for model II also lead to peak values of the KER distribution functions compared to those for model I. We note that the KER distribution functions for model II do not only differ in the tail region from those for model I (high-energy region or short-distance region), but also in the “rising portion” of the KER distribution function (large distance region); these deviations are more pronounced for larger N than for smaller N . The deviations arise because the KER distribution functions in the rising portion are not dominated by configurations in which all interparticle distances are large, but by configurations where $N - 1$ interparticle distances are large and the remaining $N(N - 1)/2 - (N - 1)$ interparticle distances are not particularly large.

IV. CONCLUSIONS

This paper presented a comprehensive study of the structural properties of small bosonic helium clusters consisting of up to $N = 10$ atoms and interacting through realistic interaction potentials. In addition to helium clusters at the physical point, characterized by a two-body s -wave scattering length that is positive and finite (and notably larger than the van der Waals length), clusters interacting with an infi-

nite s -wave scattering were investigated. To reach unitarity, the realistic helium-helium interaction potential was multiplied by an overall factor that is close to, but smaller than, one.

For comparison, the properties of the systems at the physical point and at unitarity were also calculated for an effective low-energy interaction model that was introduced in the literature [33]. The model’s strictly attractive two-body potential reproduces the two-body s -wave scattering length and two-body binding energy obtained for the HFD-HE2 potential. A strictly repulsive three-body potential is added to reproduce the three- and four-body energies obtained for the HFD-HE2 potential. Importantly, there is a difference between the effective low-energy model construction for clusters at the physical point and at unitarity. At the physical point, the requirements for matching the two-body s -wave scattering length and two-body binding energy are two distinct requirements. At unitarity, in contrast, the two requirements are equivalent, i.e., fulfilling one of these requirements implies that the other requirement is fulfilled automatically.

A detailed analysis of the structural properties at small and large length scales was presented, with a focus on comparing the results for different realistic interaction potentials and those for the HFD-HE2 potential and the effective low-energy model. Several small distance behaviors were found to be described accurately by the two-body correlation function for a purely attractive $-C_6/r^6$ potential. The small length scale behavior of the pair distribution functions for the realistic interaction models at the physical point was summarized by the two-body contact and the $(2 + 1)$ contact for each cluster

size. The two-body contacts for different realistic interaction potentials were found to be related to each other through, roughly, N -independent scaling factors. Following the spirit of Ref. [34], it would be interesting to extend the current study to larger clusters and to extract, using the liquid drop model, the bulk pair-atom contact both at the physical point and at unitarity. It would also be interesting to investigate mixed clusters that contain bosonic ${}^4\text{He}$ and fermionic ${}^3\text{He}$ atoms.

ACKNOWLEDGMENTS

Support by the National Science Foundation through Grants No. PHY-1806259 and No. PHY-2110158 is gratefully acknowledged. Work during the early stage was additionally supported by Grant No. NSF-1659501. This work used the OU Supercomputing Center for Education and Research (OSCER) at the University of Oklahoma (OU).

-
- [1] V. R. Pandharipande, S. C. Pieper, and R. B. Wiringa, *Phys. Rev. B* **34**, 4571 (1986).
- [2] V. R. Pandharipande, J. G. Zabolitzky, S. C. Pieper, R. B. Wiringa, and U. Helmbrecht, *Phys. Rev. Lett.* **50**, 1676 (1983).
- [3] R. N. Barnett and K. B. Whaley, *Phys. Rev. A* **47**, 4082 (1993).
- [4] T. K. Lim, S. K. Duffy, and W. C. Damer, *Phys. Rev. Lett.* **38**, 341 (1977).
- [5] T. Corneliuss and W. Glöckle, *J. Chem. Phys.* **85**, 3906 (1986).
- [6] K. B. Whaley, *Intl. Rev. Phys. Chem.* **13**, 41 (1994).
- [7] M. Lewerenz, *J. Chem. Phys.* **106**, 4596 (1997).
- [8] B. D. Esry, C. D. Lin, and C. H. Greene, *Phys. Rev. A* **54**, 394 (1996).
- [9] R. Guardiola, O. Kornilov, J. Navarro, and J. Peter Toennies, *J. Chem. Phys.* **124**, 084307 (2006).
- [10] J. P. Toennies, *Mol. Phys.* **111**, 1879 (2013).
- [11] S. A. Chin and E. Krotscheck, *Phys. Rev. B* **52**, 10405 (1995).
- [12] F. Dalfovo, A. Latri, L. Pricapenko, S. Stringari, and J. Treiner, *Phys. Rev. B* **52**, 1193 (1995).
- [13] Y. Kwon, P. Huang, M. V. Patel, D. Blume, and K. B. Whaley, *J. Chem. Phys.* **113**, 6469 (2000).
- [14] F. Luo, C. F. Giese, and W. R. Gentry, *J. Chem. Phys.* **104**, 1151 (1996).
- [15] W. Schöllkopf and J. P. Toennies, *Science* **266**, 1345 (1994).
- [16] W. Schöllkopf and J. P. Toennies, *J. Chem. Phys.* **104**, 1155 (1996).
- [17] R. E. Grisenti, W. Schöllkopf, J. P. Toennies, G. C. Hegerfeldt, T. Köhler, and M. Stoll, *Phys. Rev. Lett.* **85**, 2284 (2000).
- [18] E. Braaten and H.-W. Hammer, *Phys. Rev. A* **67**, 042706 (2003).
- [19] E. Hiyama and M. Kamimura, *Phys. Rev. A* **85**, 062505 (2012).
- [20] E. Hiyama and M. Kamimura, *Phys. Rev. A* **85**, 022502 (2012).
- [21] M. V. Rama Krishna and K. B. Whaley, *J. Chem. Phys.* **93**, 6738 (1990).
- [22] P. Barletta and A. Kievsky, *Phys. Rev. A* **64**, 042514 (2001).
- [23] E. Nielsen, D. V. Fedorov, and A. S. Jensen, *J. Phys. B: At., Mol. Opt. Phys.* **31**, 4085 (1998).
- [24] D. Blume, C. H. Greene, and B. D. Esry, *J. Chem. Phys.* **113**, 2145 (2000).
- [25] D. Blume, *Few-Body Syst.* **56**, 859 (2015).
- [26] M. Kunitski, S. Zeller, J. Voigtsberger, A. Kalinin, L. P. H. Schmidt, M. Schöffler, A. Czasch, W. Schöllkopf, R. E. Grisenti, T. Jahnke *et al.*, *Science* **348**, 551 (2015).
- [27] E. A. Kolganova, A. K. Motovilov, and W. Sandhas, *Few-Body Syst.* **51**, 249 (2011).
- [28] P. Stipanović, L. V. Markić, and J. Boronat, *J. Phys. B: At. Mol. Opt. Phys.* **49**, 185101 (2016).
- [29] P. Naidon, E. Hiyama, and M. Ueda, *Phys. Rev. A* **86**, 012502 (2012).
- [30] A. Kievsky, N. K. Timofeyuk, and M. Gattobigio, *Phys. Rev. A* **90**, 032504 (2014).
- [31] A. Kievsky, A. Polls, B. Juliá-Díaz, and N. K. Timofeyuk, *Phys. Rev. A* **96**, 040501(R) (2017).
- [32] D. Blume and C. H. Greene, *J. Chem. Phys.* **112**, 8053 (2000).
- [33] A. Kievsky, A. Polls, B. Juliá-Díaz, N. K. Timofeyuk, and M. Gattobigio, *Phys. Rev. A* **102**, 063320 (2020).
- [34] B. Bazak, M. Valiente, and N. Barnea, *Phys. Rev. A* **101**, 010501(R) (2020).
- [35] M. Przybytek, W. Cencek, J. Komasa, G. Łach, B. Jeziorski, and K. Szalewicz, *Phys. Rev. Lett.* **104**, 183003 (2010).
- [36] S. Zeller, M. Kunitski, J. Voigtsberger, A. Kalinin, A. Schottelius, C. Schober, M. Waitz, H. Sann, A. Hartung, T. Bauer *et al.*, *Proc. Natl. Acad. Sci.* **113**, 14651 (2016).
- [37] D. M. Ceperley, *Rev. Mod. Phys.* **67**, 279 (1995).
- [38] K. Pomorski and J. Dudek, *Phys. Rev. C* **67**, 044316 (2003).
- [39] R. P. Feynman and M. Cohen, *Phys. Rev.* **102**, 1189 (1956).
- [40] D. G. Henshaw and A. D. B. Woods, *Phys. Rev.* **121**, 1266 (1961).
- [41] M. V. Rama Krishna and K. B. Whaley, *J. Chem. Phys.* **93**, 746 (1990).
- [42] S. Grebenev, J. P. Toennies, and A. F. Vilesov, *Science* **279**, 2083 (1998).
- [43] J. P. Toennies and A. F. Vilesov, *Angew. Chem. Intl. Ed.* **43**, 2622 (2004).
- [44] A. Mauracher, O. Echt, A. Ellis, S. Yang, D. Bohme, J. Postler, A. Kaiser, S. Denifl, and P. Scheier, *Phys. Rep.* **751**, 1 (2018).
- [45] F. Bierau, P. Kupser, G. Meijer, and G. von Helden, *Phys. Rev. Lett.* **105**, 133402 (2010).
- [46] J. P. Toennies, A. F. Vilesov, and K. B. Whaley, *Phys. Today* **54**(2), 31 (2001).
- [47] F. Stienkemeier and K. K. Lehmann, *J. Phys. B: At., Mol. Opt. Phys.* **39**, R127 (2006).
- [48] C. Callegari, K. K. Lehmann, R. Schmied, and G. Scoles, *J. Chem. Phys.* **115**, 10090 (2001).
- [49] J. P. Toennies and A. F. Vilesov, *Annu. Rev. Phys. Chem.* **49**, 1 (1998).
- [50] R. A. Aziz, V. P. S. Nain, J. S. Carley, W. L. Taylor, and G. T. McConville, *J. Chem. Phys.* **70**, 4330 (1979).
- [51] W. Cencek, M. Przybytek, J. Komasa, J. B. Mehl, B. Jeziorski, and K. Szalewicz, *J. Chem. Phys.* **136**, 224303 (2012).
- [52] K. T. Tang, J. P. Toennies, and C. L. Yiu, *Phys. Rev. Lett.* **74**, 1546 (1995).
- [53] P. Naidon, S. Endo, and M. Ueda, *Phys. Rev. Lett.* **112**, 105301 (2014).
- [54] P. Naidon, S. Endo, and M. Ueda, *Phys. Rev. A* **90**, 022106 (2014).
- [55] S. Tan, *Ann. Phys.* **323**, 2987 (2008).
- [56] S. Tan, *Ann. Phys.* **323**, 2971 (2008).

- [57] S. Tan, *Ann. Phys.* **323**, 2952 (2008).
- [58] F. Werner and Y. Castin, *Phys. Rev. A* **86**, 013626 (2012).
- [59] F. Werner and Y. Castin, *Phys. Rev. A* **86**, 053633 (2012).
- [60] E. Braaten, D. Kang, and L. Platter, *Phys. Rev. Lett.* **106**, 153005 (2011).
- [61] R. Weiss, B. Bazak, and N. Barnea, *Phys. Rev. Lett.* **114**, 012501 (2015).
- [62] R. Weiss, B. Bazak, and N. Barnea, *Phys. Rev. C* **92**, 054311 (2015).
- [63] G. A. Miller, *Phys. Lett. B* **777**, 442 (2018).
- [64] O. Hen, M. Sargsian, L. B. Weinstein, E. Piasetzky, H. Hakobyan, D. W. Higinbotham, M. Braverman, W. K. Brooks, S. Gilad, K. P. Adhikari *et al.*, *Science* **346**, 614 (2014).
- [65] R. Cruz-Torres, D. Lonardonì, R. Weiss, M. Piarulli, N. Barnea, D. W. Higinbotham, E. Piasetzky, A. Schmidt, L. B. Weinstein, R. B. Wiringa *et al.*, *Nat. Phys.* **17**, 306 (2021).
- [66] D. Odell, A. Deltuva, and L. Platter, *Phys. Rev. A* **104**, 023306 (2021).
- [67] We use $\hbar^2/m = 12.119 \text{ K } \text{\AA}^2$ (the last digit is rounded). This agrees with the value used by Hiyama and Kamimura [19], but is about $6 \times 10^{-3}\%$ smaller than the value used by Kievsky *et al.* [33]. For the HFD-HE2 potential, this difference translates to differences in the two-body s -wave scattering length and the two-, three-, and four-body energies that are larger than our numerical uncertainties. Using $\hbar^2/m = 12.12 \text{ K } \text{\AA}^2$ [33], we find—in agreement with Ref. [33]— $a_s = 235.546a_0$, which is 0.3% larger than the value reported in the main part of this paper.
- [68] We note that the definition of the model in Ref. [33] contains a typographical error: Reference [33] reports w_0 as being positive; it is, however, negative. Our R_0 is related to ρ_0 through $\rho_0^2 = 12R_0^2$.
- [69] Y. Yan and D. Blume, *Phys. Rev. A* **92**, 033626 (2015).
- [70] J. von Stecher, *J. Phys. B: At., Mol. Opt. Phys.* **43**, 101002 (2010).
- [71] A. R. Janzen and R. A. Aziz, *J. Chem. Phys.* **103**, 9626 (1995).
- [72] E. Braaten and H.-W. Hammer, *Phys. Rep.* **428**, 259 (2006).
- [73] E. Braaten and H.-W. Hammer, *Ann. Phys.* **322**, 120 (2007).
- [74] P. Naidon and S. Endo, *Rep. Prog. Phys.* **80**, 056001 (2017).
- [75] L. Platter, C. Ji, and D. R. Phillips, *Phys. Rev. A* **79**, 022702 (2009).
- [76] For the interaction potentials of model I type, the effective range r_{eff} is, in the large $|a_s|$ regime, roughly three times as large as the van der Waals length r_{vdW} .
- [77] I. Kosztin, B. Faber, and K. Schulten, *Am. J. Phys.* **64**, 633 (1996).
- [78] B. M. Austin, D. Y. Zubarev, and W. A. Lester, *Chem. Rev.* **112**, 263 (2012).
- [79] C. J. Umrigar, M. P. Nightingale, and K. J. Runge, *J. Chem. Phys.* **99**, 2865 (1993).
- [80] S. W. Rick, D. L. Lynch, and J. D. Doll, *J. Chem. Phys.* **95**, 3506 (1991).
- [81] N. Metropolis, A. W. Rosenbluth, M. N. Rosenbluth, A. H. Teller, and E. Teller, *J. Chem. Phys.* **21**, 1087 (1953).
- [82] See Supplemental Material at <http://link.aps.org/supplemental/10.1103/PhysRevA.105.022824> for the imaginary-time step dependence, variational parameters, numerical values for the two-body and 2+1 contacts, and selected distribution functions.
- [83] P. J. Reynolds, R. N. Barnett, B. L. Hammond, and W. A. Lester, *J. Stat. Phys.* **43**, 1017 (1986).
- [84] R. Barnett, P. Reynolds, and W. Lester, *J. Comput. Phys.* **96**, 258 (1991).
- [85] R. A. Aziz and M. J. Slaman, *J. Chem. Phys.* **94**, 8047 (1991).
- [86] C. Lin, *Phys. Rep.* **257**, 1 (1995).
- [87] J. P. D’Incao, *J. Phys. B: At., Mol. Opt. Phys.* **51**, 043001 (2018).
- [88] J. Voigtsberger, S. Zeller, J. Becht, N. Neumann, F. Sturm, H.-K. Kim, M. Waitz, F. Trinter, M. Kunitski, A. Kalinin *et al.*, *Nat. Commun.* **5**, 5765 (2014).
- [89] B. Ulrich, A. Vredenburg, A. Malakzadeh, L. P. H. Schmidt, T. Havermeier, M. Meckel, K. Cole, M. Smolarski, Z. Chang, T. Jahnke *et al.*, *J. Phys. Chem. A* **115**, 6936 (2011).
- [90] S. Kazandjian, J. Rist, M. Weller, F. Wiegandt, D. Aslitürk, S. Grundmann, M. Kircher, G. Nalin, D. Pitters, I. Vela Pérez *et al.*, *Phys. Rev. A* **98**, 050701(R) (2018).
- [91] Y. E. Kim and A. Tubis, *Annu. Rev. Nucl. Sci.* **24**, 96 (1974).
- [92] J. L. Friar, B. F. Gibson, D. R. Lehman, and G. L. Payne, *Phys. Rev. C* **25**, 1616 (1982).
- [93] V. V. Flambaum, G. F. Gribakin, and C. Harabati, *Phys. Rev. A* **59**, 1998 (1999).
- [94] B. Gao, *Phys. Rev. A* **58**, 4222 (1998).
- [95] Y. Castin, *C. R. Phys.* **5**, 407 (2004).
- [96] F. Werner and Y. Castin, *Phys. Rev. A* **74**, 053604 (2006).
- [97] S. Jonsell, H. Heiselberg, and C. J. Pethick, *Phys. Rev. Lett.* **89**, 250401 (2002).
- [98] E. Hiyama and M. Kamimura, *Phys. Rev. A* **90**, 052514 (2014).